STRATOSPHERIC OBSERVATION OF RESIDENT SPACE OBJECTS USING PHOTOMETRIC AND INFRARED SENSORS

V. Suthakar(1), I. Porto(1), S. K. M. Dasanayaka(1), R. S. K. Lee(1), M. I. Robert(2), R. Olteanu(2), A. Bucur(2), M. Kübler(3), J. I. Hubbard(4), M. Scherillo(5), F. Newland(6), and V. Braun(7)

(1) *York University, Toronto, ON M3J 1P3, Canada, {vithurs, ianporto, kaveenm, reginal}@yorku.ca*
(2) *Romanian InSpace Engineering (RISE), Măgurele 077125, Romania, {miron.robert.ionut, bucur3215, raduiolteanu}@gmail.com*
(3) *TU Darmstadt, 64289 Darmstadt, Germany, melina.kuebler@outlook.com*
(4) *Queen Mary University of London, London E1 4NS, United Kingdom, joosthubbard@gmail.com*
(5) *University of Naples Federico II, 40, 80138 Napoli NA, Italy, marta.scherillo28@gmail.com*
(6) *University of Ottawa, Ottawa, ON K1H 8M5, Canada, franz.newland@uottawa.ca*
(7) *IMS Space Consultancy GmbH at ESA/ESOC Space Debris Office, Darmstadt, Germany, vitali.braun@esa.int*

ABSTRACT

The Low Earth Orbit (LEO) environment has expanded rapidly in recent years due to standardization, miniaturization, and increasing commercial activity. With launch traffic reaching record highs and the deployment of large satellite constellations, the growing population of Resident Space Objects (RSOs)—including satellites, defunct spacecraft, and debris—poses risks to space operations and astronomical observations. Even small-scale objects can generate hazardous collisions, as demonstrated by the Sentinel-1A incident in 2016. Effective tracking and cataloging are therefore essential for Space Situational Awareness (SSA).

This paper introduces the Space Object Brightness Evaluation and Reference (SOBER) mission, an SSA initiative leveraging optical and infrared observations from a stratospheric balloon platform. Operating above 25 km, this platform minimizes atmospheric interference, enabling more precise RSO brightness measurements. This study serves as a performance evaluation of three key sensors—PCO and BFS (optical), and Radia (infrared)—using Systems Tool Kit (STK) simulations informed by historical flight data. Tracking duration, signal-to-noise ratio, and spatial resolution were analyzed to assess each sensor's suitability for future SSA missions.

A correlation analysis was conducted between simulated detections and existing SSA datasets, including ESA's DISCOS database, the GCAT catalog, and public photometric repositories. This approach enabled the validation of observed RSOs, the identification of uncharacterized debris fragments, and the enhancement of RSO profiles through data fusion.

By capturing both reflected and emitted radiation, SOBER characterizes the impact of space debris and atmospheric light pollution on astronomical observations, supporting ESA's Zero Debris policy and the Dark & Quiet Skies initiative. The mission payload includes optical and infrared sensors undergoing technology demonstration, selected for their potential to image RSOs and gain in-flight validation for future in-orbit deployments.

SOBER will measure the photometric and astrometric properties of RSOs across multiple spectral bands. The optical sensor will quantify brightness in visible bands, providing data on reflectivity, visual magnitude, and attitude stability. Meanwhile, the thermal sensor will capture emitted infrared Radiation, offering insights into material composition and differentiating between active satellites and inert debris.

By integrating optical and thermal sensor data, SOBER will provide comprehensive RSO brightness profiles, significantly enhancing SSA capabilities. This multispectral approach supports ESA's Zero Debris policy by providing critical data to inform mitigation strategies, reduce artificial light pollution, and preserve dark skies.

Keywords: Space Situational Awareness (SSA); Resident Space Objects (RSOs); Stratospheric Observations.

1. INTRODUCTION

In recent decades, the space sector has experienced unprecedented growth, driven by the rapid commercialization and miniaturization of satellites. Government-led space exploration is increasingly complemented by private enterprises launching satellites for communications, Earth observation, and scientific research. The advent of small satellites, including CubeSats and other nanosatellites, has significantly lowered the barriers to entry, enabling a surge in satellite production and deployment.

Proc. 9th European Conference on Space Debris, Bonn, Germany, 1–4 April 2025, published by the ESA Space Debris Office
Editors: S. Lemmens, T. Flohrer & F. Schmitz, (http://conference.sdo.esoc.esa.int, April 2025)

This expansion has resulted in a growing population of Resident Space Objects (RSOs)—a term encompassing all objects in Earth's orbit, including operational and defunct satellites, rocket bodies, and space debris. With launch rates reaching record highs, space has become increasingly congested, complicating space traffic management and creating significant sustainability concerns.

The accumulation of RSOs poses several challenges that have implications for space operations and ground-based activities. In Low Earth Orbit (LEO), relative velocities typically range between 8 and 12 km/s, significantly higher than in geosynchronous orbit (GEO). Hence, a collision between two objects would likely result in their complete destruction, generating additional debris and potentially contributing to a worsening collisional cascading effect. As the number of objects in orbit increases, the probability of accidental impacts rises, potentially generating additional debris and leading to a destructive chain reaction, a scenario often referred to as the Kessler Syndrome.

Additionally, the reflective surfaces of satellites and debris scatter sunlight, increasing the brightness of the night sky, which can interfere with astronomical observations. This phenomenon, known as space-induced light pollution, reduces the visibility of faint celestial objects, hindering both professional and amateur astronomical research. Mitigating these effects requires improved imaging capabilities, particularly in understanding the photometric properties of RSOs. The Space Object Brightness Evaluation and Reference (SOBER) mission contributes to this goal by leveraging multispectral observations to enhance RSO classification, improve debris mitigation, and support sustainable space operations.

As of March 2025, Space Surveillance Networks worldwide actively track approximately 39,340 RSOs[1]. Additionally, statistical models from MASTER-8 suggest that between 1,100,000 and 1,200,000 objects (ranging from 1 cm to 10 cm) exist in orbit. Debris of this scale poses a significant threat, as demonstrated by the Sentinel-1A collision in August 2016 [2].

Despite extensive Space Situational Awareness (SSA) monitoring, a major gap remains: current systems lack comprehensive multispectral brightness profiles, limiting the ability to characterize the optical and thermal properties of RSOs. SOBER addresses this challenge by combining optical and infrared imaging to obtain detailed brightness measurements of RSOs, improving SSA tracking and brightness modeling. Using Systems Tool Kit (STK) simulations, we assess the effectiveness of SOBER's optical and infrared sensors, demonstrating that optical sensors are optimal for long-duration RSO brightness measurements, while infrared sensors provide precise thermal emission data for space debris. These insights directly inform sensor selection, payload design, and data processing strategies, ensuring optimized SSA mission planning.

As part of the Balloon-borne Experiments for University Students (BEXUS) Launch Campaign in October 2025, SOBER will be deployed at the Swedish Space Corporation (SSC) Esrange/Kiruna, Sweden. Using a stratospheric balloon platform, it will collect infrared and visible imaging data of RSOs. By operating above most of Earth's atmosphere, this approach mitigates atmospheric distortion, ensuring more precise photometric measurements.

The collected data will be cross-referenced with ESA's Database and Information System Characterising Objects in Space (DISCOS) database, improving brightness modelling for RSOs and contributing to satellite design optimizations in early development phases. By integrating observational data with DISCOS, SOBER enhances the photometric properties of RSOs, particularly for uncharacterized debris fragments, directly supporting ESA's Zero Debris policy and long-term SSA sustainability. This study provides an overview of the SOBER mission, detailing both the hardware and software development of the payload, which form the foundation for its observational capabilities. The primary objective is to assess sensor performance in a near-space environment, improve SSA data modeling, and contribute to ESA's DISCOS database for enhanced debris tracking and mitigation.

2. SOBER HARDWARE OVERVIEW

The SOBER payload is designed to meet mission objectives while withstanding the harsh conditions of stratospheric flight. As illustrated in Figure 1, the payload follows a CubeSat structural design, which consists of three modular units: a) Infrared module – houses the infrared camera, b) Electronics module – holds the power distribution unit, onboard computer (OBC), and other electronics c) Optical module – contains the visible spectrum camera. This modular approach enables rapid assembly and disassembly, which is critical for pre-flight testing and integration. The payload frame is mounted at a 45° elevation, ensuring an unobstructed field of view (FOV), an approach previously employed in stratospheric SSA missions [3, 4].

2.1. Sensors

The optical sensor (BFS) [5] captures images in the $400-700\,\mathrm{nm}$ range, featuring adaptive exposure control to accommodate varying light conditions via telemetry. The infrared camera (Radia) [6], developed by Telops, operates in the $3.6-4.15\,\mu\mathrm{m}$ band with a thermal sensitivity of $30\,\mathrm{mK}$, enabling detailed thermal imaging. To ensure precise positioning and pointing accuracy, the payload integrates an Inertial Measurement Unit (IMU) that fuses data from a triaxial 16-bit gyroscope, a triaxial 14-bit accelerometer and a full-performance geomagnetic sensor. The IMU data will be combined with Global Navigation Satellite System (GNSS) telemetry from the

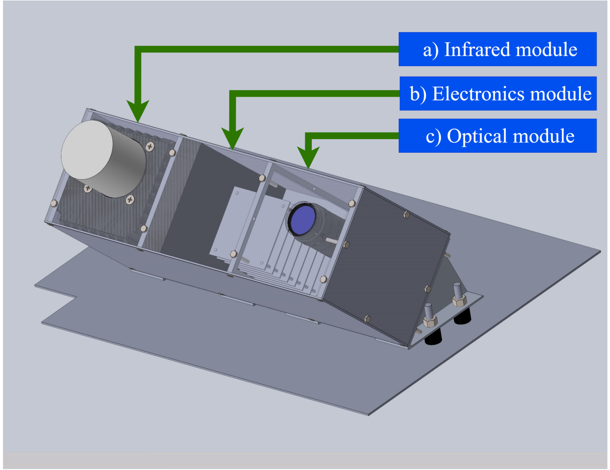

Figure 1. Computer Aided Design model of the SOBER payload, showing its modular structure. The system is divided into three primary components: (a) Infrared module, (b) Electronics module, and (c) Optical module.

BEXUS gondola, allowing for accurate attitude reconstruction and timestamp correlation with imaging data.

2.2. Electronics

The system integrates a Raspberry Pi Compute Module 4 as the OBC, managing all system operations, data acquisition, and storage [7]. It is responsible for interfacing with sensors, processing the collected data, and executing the control logic for the experiment. Additionally, it manages communication between subsystems and logs environmental parameters for post-flight analysis. The Raspberry Pi Compute Module 4 is mounted on a dedicated PC/104 CubeSat-format PCB (motherboard). The motherboard includes one GbE (Gigabit Ethernet) RJ-45 port for fast and reliable network connectivity, two USB 3.0 Type-A sockets for high-speed data transfer, and Raspberry Pi HAT and power connectors. It also includes an SD card slot for data storage.

The payload is powered by a 24 – 34 V / 3 A supply provided by the BEXUS gondola. Power distribution is managed through a dedicated Power Distribution Module (PDM), which consists of:

- 5 V – Powers the onboard computing system.
- 3.3 V – Supports the environmental sensors and IMU.
- 12 V – Supplies power to the infrared and optical cameras.

Figure 2 illustrates the electrical system architecture, including power distribution, subsystem communication pathways, and connectivity.

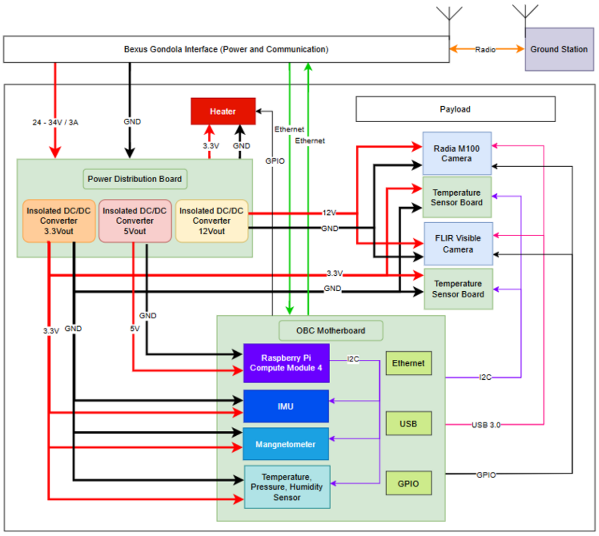

Figure 2. Electrical system architecture of the SOBER payload. The diagram illustrates the power distribution from the BEXUS gondola interface, communication pathways, and connectivity between onboard subsystems.

2.3. Calibration

Calibration of imaging sensors is essential to ensure accurate and reliable in-flight measurements. The infrared sensor is calibrated using a blackbody reference source, while a stable LED light source is used for the optical sensor. The infrared sensor undergoes extensive testing to compensate for thermal lens offsets, characterizing corrections across different temperature conditions.

To account for optical distortions, such as barrel distortion, Zhang's camera calibration algorithm is applied using a checkerboard pattern [8]. Noise reduction techniques are employed to correct thermal and electronic irregularities that arise in low-light and infrared imaging. Bias frames are used to capture read-out noise, while dark frames are collected in complete darkness at varying temperatures and exposure rates. These calibration frames are subtracted from flight data to improve image fidelity and mitigate sensor-induced artifacts, especially in long-exposure or infrared images.

Environmental factors, including pressure variations and condensation, are critical considerations. Rapid pressure changes may compromise the integrity of the optical system, while condensation or ice formation on the lens can degrade image quality. Previous RSONAR missions did not report significant issues with these factors, as documented in a lessons learned study [9]; however, ESA-mandated thermal and vacuum testing is still required to validate the robustness of the SOBER payload.

Simulated flight conditions, including lighting variations, will use previous BEXUS flight data to optimize exposure settings for the imaging system. The exposure rate will be preset based on these simulations and experimental evaluations of limiting magnitudes from field campaigns. Adjustments, if necessary, can be made via ground station uplink commands.

2.4. Environmental and Structural Protection

To monitor operational stability in the extreme stratospheric environment, where temperatures can drop as low as $-80\,^{\circ}\mathrm{C}$, the payload incorporates a network of temperature, pressure, and humidity sensors to continuously track internal conditions. Additionally, an active heating system is integrated to maintain optimal sensor performance, prevent lens condensation, and stabilize imaging electronics. Heat sinks and internal insulation facilitate efficient thermal dissipation between components, reducing the risk of performance degradation. To protect sensitive components from shock and vibrations, mechanical shock absorbers are integrated into the payload interfaces, ensuring structural integrity during balloon ascent and descent.

3. SOBER SOFTWARE OVERVIEW

The onboard software is responsible for sensor monitoring, data acquisition, and communication with the ground station, while ensuring safe system operation. Running on the Raspberry Pi 4, it follows a structured operational approach. Upon startup, the system performs self-tests to verify peripheral communication and awaits input to initiate the experiment. Once the necessary parameters are received from the ground station, the software configures the imaging system by adjusting camera settings. Captured images are stored in onboard memory and transmitted later for quality assessment and optimization.

Figure 3 illustrates the SOBER payload's software architecture, depicting the interaction between the ground station, the gondola's E-Link system, the OBC, and peripheral devices. The ground station transmits commands to modify camera parameters, retrieve sensor health data, and adjust imaging conditions based on real-time feedback. The Command Dispatcher functions as a Script Handler, interpreting commands and executing control over peripherals according to the experiment's logic.

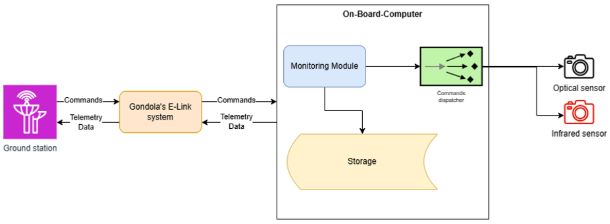

Figure 3. Software architecture of the SOBER payload. The diagram illustrates the interaction between the ground station, the gondola's E-Link communication system, and the onboard computer.

3.1. Communication Infrastructure

The ESA-provided E-Link system facilitates real-time data exchange between the ground segment and the payload. The ground station consists of an antenna, an antenna controller, and a Monitor & Control Unit, while the airborne system includes an antenna, a battery, an RF interface unit, and the main unit. Each experimenter is provided with a dedicated Ethernet connection, allowing periodic transmission of environmental data and on-demand image retrieval.

As displayed in Figure 4, the ground station module plays a central role in experiment management and data transmission. Operators can configure camera parameters—such as frame rate, exposure, and resolution—to optimize imaging under varying lighting conditions. Additionally, it displays real-time environmental data, such as camera temperatures, internal payload temperature, humidity, and pressure. The ground station also enables direct image retrieval from the infrared and optical sensors, allowing for real-time image quality evaluation. This ensures that the payload captures relevant observational data, supporting subsequent scientific analysis.

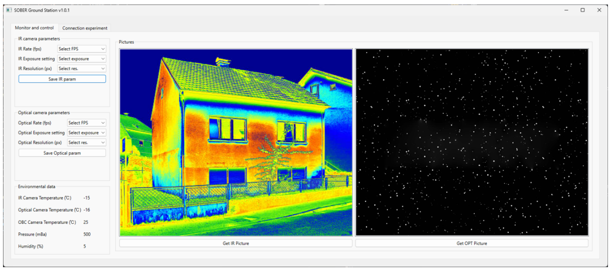

IR Rate (fps) Select FPS
IR Exposure setting Select exposure
IR Resolution (px) Select res.
Optical Rate (fps) Select FPS
Optical Exposure setting Select exposure
Optical Resolution (px) Select res.
IR Camera Temperature (°C) -15
Optical Camera Temperature (°C) -16
OBC Camera Temperature (°C) 25
Pressure (mBa) 500
Humidity (%) 5

Figure 4. SOBER Ground Station Interface. The left panel allows operators to configure frame rates, exposure settings, and resolution for each sensor [10]. The right panel displays live images captured by the IR and optical cameras [11]. The system also logs temperature, pressure, and humidity data to ensure operational stability.

4. METHODOLOGY

To accurately simulate sensor performance during stratospheric flight, realistic environmental and positional data from the RSONAR mission [12] was incorporated into the STK simulation environment. The dataset acquired from RSONAR was used to validate the simulation setup by comparing real images from the mission with synthetic images generated using STK's EOIR model [13]. The RSOs detected in the RSONAR dataset were also present in the simulated images, confirming the simulation's fidelity.

Beyond its role in simulation, the RSONAR dataset has supported multiple downstream applications in the SSA domain. It has enabled the development and validation of a traditional frame differencing algorithm [12] for onboard deployment on FPGA platforms in the upcoming RSONAR mission (R3). Additionally, it has contributed to the creation of ORBIT, an open-source, web-based platform for RSO detection and annotation. ORBIT integrates automated detection in optical imagery with human-in-the-loop validation through an interactive graphical interface. The dataset has also supported the training and evaluation of 3D convolutional neural network and streak detection techniques for enhanced RSO identification in optical data streams.

The trajectory was defined using gondola pointing data and GPS information provided by CNES under the STRATO-SCIENCE 2022 framework, in collaboration with the CNES/CSA Agreement for the 22 August 2022 flight [14]. The analysis focused on the period 08:00–09:00 UTC (astronomical dawn), the optimal time for RSO observations due to favorable phase angles between the target and the observer.

Analysis of latitude-longitude-altitude (LLA) data confirmed a stable stratospheric trajectory as presented in figure 5, with altitude consistently maintained between 36–37 km. Minimal lateral drift was observed, with latitude ranging from 48.72° N to 48.90° N and longitude from -82.20° W to -81.85° W, ensuring near-stationary conditions for an airborne observer. Solar illumination angles relative to the sensor remained at approximately 90° throughout the observation period, reducing direct solar interference and preventing sensor saturation. These favourable lighting conditions were critical for precise optical sensor measurements. This combination of stable altitude, minimal drift, and consistent solar illumination ensured that the historical flight data served as realistic inputs for predicting sensor performance and validating the simulation framework.

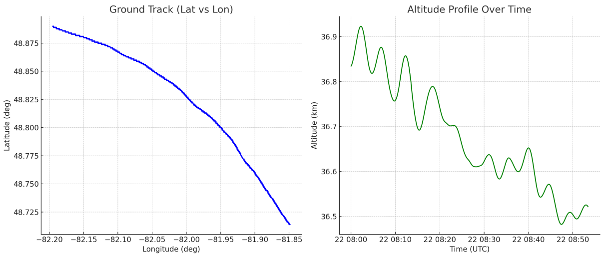

Figure 5. Trajectory and altitude profile during the simulation period. Left: Ground track showing latitude vs. longitude. Right: Altitude variation over time.

4.1. Sensor Configuration

The optical system (PCO) from the RSONAR mission was used in this study to compare and contrast sensor performance against those selected for SOBER.Table 1 summarizes the key sensor parameters used in the simulation. The FOV, pixel pitch, and optical properties for the PCO, BFS, and Radia sensors were implemented according to their datasheets and mission requirements.

Table 1. Sensor parameters for PCO, BFS, and Radia sensors used in the simulation.

Sensor Parameters	PCO	BFS	Radia
FOV (deg)	29.7 × 29.7	12.6 × 12.6	14.6 × 11.7
Pixel Pitch (μm)	6.5	3.45	10
Wavelength (μm)	0.4–0.7	0.4–0.7	3.6–4.15
Diffraction Wavelength (μm)	0.55	0.55	3.87
Integration Time (ms)	100	100	100

4.2. Assumptions and Scope

The current simulation makes several simplifying assumptions. Firstly, detailed sensor noise parameters, particularly the quantum efficiency, dark current, and readout noise for sensors Radia and BFS, were unavailable. The quantum efficiency of the sensors is especially critical, significantly impacting their sensitivity across various wavelength bands. Therefore, actual sensor performance during flight may differ from simulated predictions, depending on these factors.

Secondly, atmospheric interference was not modeled explicitly due to the operational altitude of the RSONAR flight (approximately 36–37 km), which is above most atmospheric interference. However, for the planned ESA BEXUS flight campaign, the balloon is expected to operate at lower altitudes (around 25 km), where residual atmospheric effects—though significantly reduced—could still affect optical and infrared sensor performance. Thus, future analyses, particularly those aimed at lower-altitude balloon flights, should incorporate appropriate atmospheric attenuation and scattering models to account for potential impacts on detection thresholds and image quality.

Thirdly, unlike RSONAR, the BEXUS balloon platform does not provide active stabilization or precise pointing control. As a result, the sensor performance observed in the current simulation—based on stabilized pointing conditions—may not fully reflect the dynamic behavior of the payload during the actual BEXUS flight. Future simulation efforts will incorporate passive pointing drift and BEXUS-specific trajectory models to more accurately predict in-flight imaging conditions and refine the expected observational performance.

5. RESULTS

5.1. Sensor Access Duration and Distribution

The duration for which RSOs remain within a sensor's FOV is dictated by orbital mechanics and sensor geometry. Higher-altitude RSOs in LEO travel at lower velocities, leading to longer access durations. Since the sensors passively observe objects transiting through their FOV with minimal lateral and pointing drift, access time is dictated by the intersection of the orbital path with the sensor's FOV.

During the simulation, PCO, BFS, and Radia recorded detections of 408, 171, and 177 LEO objects, respectively. A detailed classification of these detections is presented in Section 5.3. Figure 6 presents violin plots illustrating the access duration distribution for each sensor (PCO, BFS, and Radia), highlighting observational variability and differences in detection performance. In Figure 6, each violin plot illustrates the density distribution of observation durations, with dashed lines marking the 25th, 50th (median), and 75th percentiles.

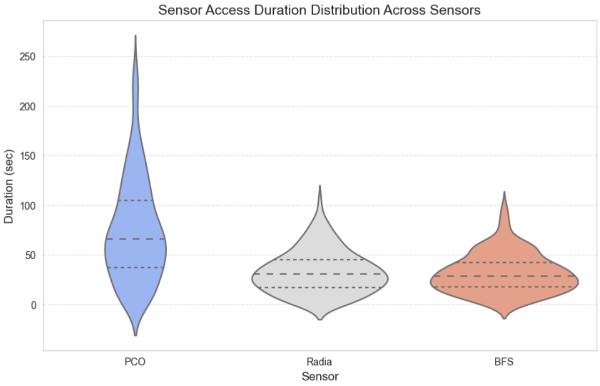

Figure 6. Violin plot illustrating access duration distributions for PCO, BFS, and Radia. Dashed lines indicate the 25th, 50th (median), and 75th percentiles.

As shown in Figure 6, PCO exhibits the longest observed access durations, occasionally exceeding 250 seconds, with a broad distribution indicating high variability. Radia and BFS, in contrast, exhibit compact distributions, with most access durations below 50 seconds, indicating their suitability for short-duration observations.

The comparative analysis of sensor access durations using an Empirical Cumulative Distribution Function (ECDF) is provided in Figure 7. The ECDF represents the probability of an observation lasting less than or equal to a given duration. A steeper curve indicates that most durations cluster around a specific range.

Radia and BFS exhibit steep slopes, confirming that the majority of their access durations are short, mostly under 50 seconds. PCO, however, displays a more gradual slope, reinforcing its ability to sustain observations over longer periods. The overlapping behavior of Radia and BFS in both the violin plot and ECDF suggests their similar performance in short-duration observations.

Both analyses confirm that PCO is optimal for long-duration SSA observations, while Radia and BFS are more effective for short-duration detections. These findings provide critical insights into the suitability of each sensor for various SSA applications.

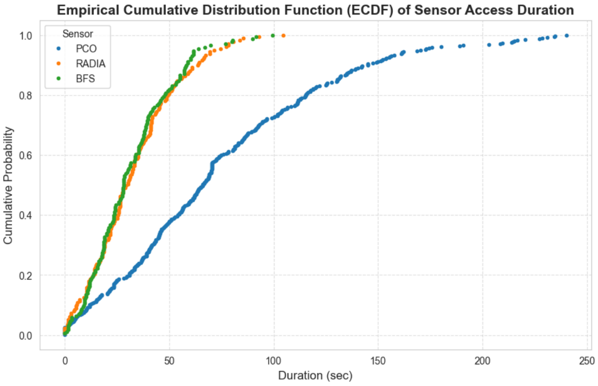

Figure 7. Empirical Cumulative Distribution Function (ECDF) comparing access durations across different sensors.

Informed by the sensor performance analysis, the team selected a 50 mm focal length lens from Thorlabs [15] for the optical camera. This configuration provides an estimated field of view of approximately $16^\circ \times 11^\circ$, offering a balanced trade-off between angular coverage and spatial resolution for effective RSO detection during stratospheric observations.

5.2. Sensor to Target Metrics

The detection and imaging capabilities of the optical and infrared sensors were evaluated using STK EOIR simulations to generate key sensor-to-target metrics, including target distance, signal-to-noise ratio (SNR), and effective instantaneous field of view (EIFOV).

For this analysis, the 20 RSOs with the longest access durations for each sensor were selected. A one-minute time step was applied, producing multiple data points for RSOs with extended observation periods. PCO captured the most data points due to its longer tracking capability and ability to detect more distant objects.

5.2.1. Signal-to-Noise Ratio (SNR) vs. Target Distance

As indicated in Figure 8, there is a clear negative correlation between signal-to-noise ratio and target distance across sensors, where SNR decreases as distance increases due to signal attenuation over longer ranges. The best-fit line equations (1), (2), and (3) for each sensor quantify this trend:

$$\mathrm{SNR}_{\mathrm{PCO}} = -0.0022 \times (\text{target distance}) + 8.2463 \quad (1)$$

$$\mathrm{SNR}_{\mathrm{Radia}} = -0.0001 \times (\text{target distance}) + 0.1477 \quad (2)$$

$$\mathrm{SNR}_{\mathrm{BFS}} = -0.0052 \times (\text{target distance}) + 14.5332 \quad (3)$$

These values indicate that PCO maintains higher SNR levels over greater distances, making it well-suited for long-range RSO tracking. In contrast, Radia consistently demonstrates low SNR values, limiting its effective detection range.

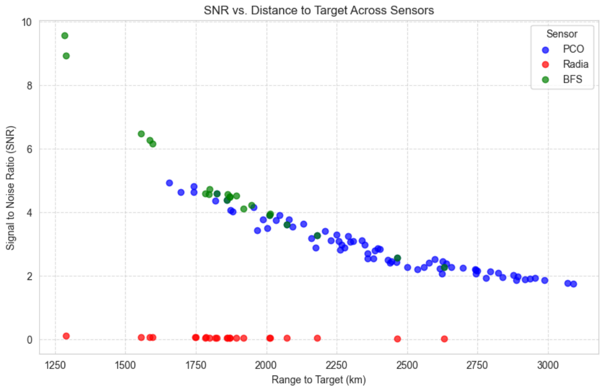

Figure 8. SNR vs. target distance for different sensors.

5.2.2. Effective Instantaneous Field of View (EIFOV) vs. Target Distance

The Effective Instantaneous Field of View (EIFOV) defines the angular extent observed by a single detector element, influencing both spatial resolution and target identification capabilities. The relationship between the EIFOV and target distance for each sensor is illustrated in Figure 9, showing variations in spatial resolution capabilities.

PCO exhibits a linear increase in EIFOV footprint with range, indicating a consistent field-of-view expansion. With an FOV of 29.7° × 29.7°, PCO effectively balances resolution and sensitivity, enabling wide-field observations while maintaining strong RSO tracking capabilities. Its steady EIFOV growth pattern makes it well-suited for long-term multi-RSO tracking without significant resolution loss.

Radia, in contrast, exhibits a steeper EIFOV increase, indicating rapid expansion of the observed scene at greater distances. With an FOV of 14.6° × 11.7° and a larger pixel pitch of 10 μm, Radia prioritizes broad scene capture over resolution, making it highly sensitive to thermal emissions but less effective for high-detail imaging.

BFS maintains the smallest EIFOV footprint, exhibiting minimal change in EIFOV size with increasing range. Its narrow FOV of 12.6° × 12.6° and smallest pixel pitch of 3.45 μm optimize it for precision tracking rather than wide-area scanning. Its stable EIFOV pattern suggests that BFS is best suited for high-resolution imaging of specific targets rather than wide-area monitoring.

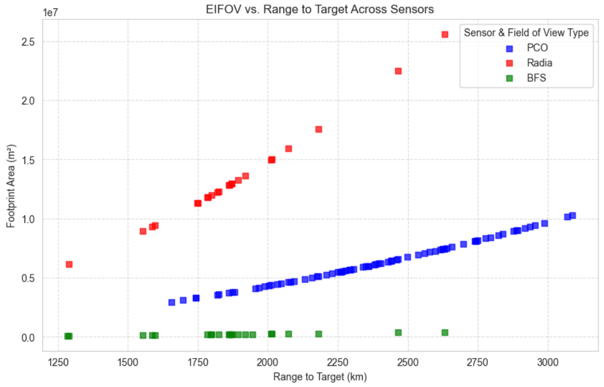

Figure 9. EIFOV vs. Range to Target Across Sensors.

5.3. Correlation with DISCOS and External Datasets

Following the access analysis, the NORAD IDs of observed RSOs were cross-referenced with ESA's DISCOS database to retrieve information on mass, dimensions, and cross-sectional areas (CRS) [16]. These attributes are essential for brightness modelling and RSO classification.

The heatmap in Figure 10 visualizes the distribution of RSO classifications across sensors based on ESA's DISCOS database. Unidentified objects were further validated using the GCAT catalog [17], confirming their classification as space debris.

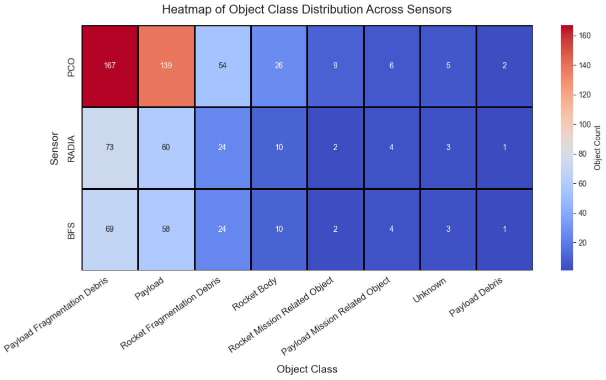

Figure 10. Heatmap of object class distribution across sensors based on ESA DISCOS data. The color scale represents the number of RSOs detected within each category.

PCO, BFS, and Radia exhibited different tracking capabilities, as analyzed in Section 5.2. These differences influence their ability to correlate with external SSA datasets, which is further explored in this section.

To further validate these findings, the NORAD IDs were also cross-referenced with external RSO photometric databases. The Mini Mega Tortora (MMT) catalog contains 12,972 RSOs with photometric measurements, including range and phase angles relative to the observer [18]. The Space Debris Light Curve Database (SDLCD) features 2,224 light curves of RSOs, aiding in object classification [19]. Additionally, the Ukrainian Database and Atlas of Light Curves provides brightness data for 340 LEO RSOs recorded between 2012 and 2020 [20]. The ASTRIANet Data for: Cosmos-1408 dataset contains optical observations of debris fragments generated by the anti-satellite test involving COSMOS-1408 [21]. Table 2 presents a comparison of cross-sectional areas from DISCOS with photometric data from these external sources.

Table 2. Comparison of DISCOS cross-sectional area data with photometric datasets from MMT, SDLCD, the Ukrainian database, and ASTRIANet for RSOs detected by each sensor.

Sensor (Observed RSOs)	PCO (408)	BFS (171)	Radia (177)
DISCOS CRS	170	72	74
MMT	131	54	56
SDLCD	2	2	2
Ukrainian Database	6	4	4
ASTRIANet	49	18	19

The cross-validation process demonstrated that while many RSOs observed by PCO, BFS, and Radia had known photometric properties, some lacked corresponding cross-sectional area data in DISCOS. For instance, PCO imaged 131 RSOs whose photometry was present in MMT, but only 118 of these RSOs had corresponding cross-sectional values in DISCOS. In addition, debris fragments from COSMOS-1408 currently do not have cross-sectional area values listed in DISCOS. Thus, observational data from the RSONAR mission and the ASTRIANet dataset can provide valuable complementary information to enhance the completeness of the DISCOS database. These findings highlight persistent data gaps in DISCOS, particularly for uncharacterized debris fragments, and underscore the importance of complementary observational datasets.

Notably, debris objects constitute approximately 55% of all RSOs observed across the sensors. However, cross-sectional area data for such debris fragments is often missing from ESA's DISCOS database — a limitation that is well recognized for non-cooperative or fragmented objects. In this context, the observational datasets provided by stratospheric SSA missions become especially valuable. By capturing photometric and infrared measurements of debris that currently lack detailed physical characterization, SOBER offers a complementary data stream that can augment DISCOS and improve the fidelity of space object modelling, debris tracking, and risk assessment. By integrating stratospheric observations with external SSA datasets, these findings help enhance the completeness and accuracy of ESA's DISCOS database, ensuring better long-term tracking of space debris.

6. CONCLUSION

This study assessed the imaging capabilities of PCO, BFS, and Radia for a stratospheric SSA mission. PCO excelled in long-duration tracking, while BFS and Radia specialized in high-precision, short-term detections. These insights contribute to the enhancement of SSA strategies for future space debris monitoring efforts. Findings from the SOBER experiment will enhance existing SSA databases, such as DISCOS, by providing validated optical and infrared data on RSOs. Future efforts will focus on sensor calibration, atmospheric corrections, and dataset integration to ensure continued improvements in space debris tracking and mitigation.

Beyond technical contributions, SOBER offers direct benefits to satellite operators, astronomers, and policy-makers. For operators, enhanced tracking data improves conjunction assessments and maneuver planning. For astronomers, SOBER's brightness measurements help quantify space-induced light pollution and preserve dark skies. For policy-makers, integration with DISCOS supports ESA's Zero Debris Policy by offering empirical data to inform regulatory frameworks. Additionally, validated sensor performance supports future SSA mission planning and guides investment in next-generation monitoring infrastructure.

6.1. Next Steps for SOBER

The SOBER mission has recently completed its Preliminary Design Review (PDR) and is preparing for the Critical Design Review (CDR) at the ESA's European Space Research and Technology Centre (ESTEC). Major subsystems are progressing toward final design, prototyping, and manufacturing, with parallel development of the ground station and post-processing software. Additional efforts focus on finalizing post-processing software, preparing for the Test Readiness Review (TRR), and establishing comprehensive operational and logistical plans for later project stages. The scientific methodology of the project is also being refined to ensure optimal data acquisition and analysis during flight operations. By incorporating simulation-based analysis and historical stratospheric SSA mission data into payload development, SOBER enhances SSA capabilities, improves RSO monitoring, and contributes to space sustainability efforts.

ACKNOWLEDGMENTS

The SOBER team acknowledges the collaboration and support of TelOps, ABB, RISE, and Velocity at Waterloo for their contributions to payload development. This research was conducted as part of the BEXUS 37 program, and we recognize the European Space Agency (ESA) and the Swedish Space Corporation (SSC) for their continued support in providing the experimental platform. Additionally, Andreas Poimenidis is acknowledged for his contributions to the mechanical interface design.

The authors contributed to various aspects of this work. V. Suthakar was responsible for conceptualization, methodology, validation, formal analysis, and visualization. I. Porto and S.K.M. Dasanayaka conducted the simulations, while V. Suthakar, M.I. Robert, R. Olteanu, A. Bucur, M. Kubler, J.I. Hubbard, and M. Scherillo contributed to the original draft preparation. R.S.K. Lee, F. Newland, and V. Braun participated in review and editing, and F. Newland provided supervision.

The RSONAR dataset used in this study is available from the corresponding author upon request.

REFERENCES

1. ESA, (2025). DISCOSweb Statistical Database, *Database and Information System Characterising Objects in Space (DISCOS)*, European Space Agency, accessed March 2025, https://sdup.esoc.esa.int/discosweb/statistics/
2. Krag H., Serrano M., Braun V., Kuchynka P., Catania M., Siminski J., Schimmerohn M., Marc X., Kuijper D., Shurmer I., O'Connell A., Otten M., Muñoz I., Morales J., Wermuth M., McKissock D., (2017). A 1 cm space debris impact onto the Sentinel-1A solar array, *Acta Astronautica*, **137**, 434–443
3. Kunalakantha P., Baires A. V., Dave S., Clark R., Chianelli G., Lee R. S. K., (2023). Stratospheric Night Sky Imaging Payload for Space Situational Awareness (SSA), *Sensors*, **23**(14), 6595
4. Qashoa R., Suthakar V., Chianelli G., Kunalakantha P., Lee R. S. K., (2024). Technology Demonstration of Space Situational Awareness (SSA) Mission on Stratospheric Balloon Platform, *Remote Sensing*, **16**(5), 749
5. Edmund Optics, (2024). BFS-U3-122S6C-C USB3 Blackfly® S Color Camera Specifications, *Edmund Optics Product Catalog*, accessed March 2025.
6. Exosens, (2024). Radia M100 Camera Specifications, *Exosens Technical Datasheet*, accessed March 2025.
7. Chianelli G., Kunalakantha P., Myhre M., Lee R. S. K., (2023). A Dual-Purpose Camera for Attitude Determination and Resident Space Object Detection on a Stratospheric Balloon, *Sensors*, **24**(1), 71
8. Zhang Z., (2004). Camera calibration with one-dimensional objects, *IEEE Transactions on Pattern Analysis and Machine Intelligence*, **26**(7), 892–899
9. R. Qashoa, P. Kunalakantha, G. Chianelli, V. Suthakar, and R. S. K. Lee, "Lessons Learned From Technology Demonstration of Space Situational Awareness (SSA) Mission," 38th Annual AIAA/USU Conference on Small Satellites (SmallSat 2024), https://digitalcommons.usu.edu/smallsat/2024/all2024/144/
10. Unblast, (2025). Free Night Sky Star Patterns, *Unblast Design Resources*, accessed March 2025.
11. iStock, (2025). Thermovision image of a house, *iStock Photo*, accessed March 2025.
12. Suthakar V., Sanvido A. A., Qashoa R., Lee R. S. K., (2023). Comparative analysis of resident space object (RSO) detection methods, *Sensors*, **23**(24), 9668
13. Analytical Graphics Inc. (AGI), (2025). EOIR Product Specification Sheet, *AGI Technical Datasheet*, accessed March 2025.
14. Canadian Space Agency (CSA), (2022). Stratospheric Balloon Campaign 2022, *Canadian Space Agency Website*, accessed March 2025.
15. Thorlabs Inc., *MVL50 - 50 mm Focal Length, VIS-NIR Fixed Focal Length Lens*, accessed March 2025. Available: `https://www.thorlabs.com/thorproduct.cfm?partnumber=MVL50`
16. ESA, (2025). DISCOSweb – Database and Information System Characterising Objects in Space, *European Space Agency Space Debris Office*, accessed March 2025, `https://discosweb.esoc.esa.int/`
17. McDowell J. C., (2020). General Catalog of Artificial Space Objects, Release 1.6.1, accessed March 2025.
18. Karpov S., Katkova E., Beskin G., Biryukov A., Bondar S., Davydov E., Ivanov E., Perkov A., Sasyuk V., (2016). Massive photometry of low-altitude artificial satellites on Mini-Mega-TORTORA, *Revista Mexicana de Astronomia y Astrofisica*, **48**, 112–113
19. Šilha J., Krajčovič S., Zigo M., Tóth J., Žilková D., Zigo P., Kornoš L., Šimon J., Schildknecht T., Cordelli E., et al., (2020). Space debris observations with the Slovak AGO70 telescope: Astrometry and light curves, *Advances in Space Research*, **65**(8), 2018–2035
20. Koshkin N., Savanevych V., Pohorelov A., Shakun L., Zhukov V., Korobeynikova E., Strakhova S., Moskalenko S., Kashuba V., Krasnoshchokov A., (2017). Ukrainian database and Atlas of light curves of artificial space objects, *Odessa Astronomical Publications*, (30), 226
21. Feige-Malan S., Karpov S., Beskin G., Katkova E., Biryukov A., Bondar A., Ivanov E., (2021). ASTRIANet Data for: Cosmos-1408, *ASTRIANet Database*, version V2, accessed March 2025, `https://doi.org/10.18738/T8/PYWBDN`